Journal of the European Ceramic Society 22 (2002) 2647–2655
www.elsevier.com/locate/jeurceramsoc

Microstructural and microchemical analysis of the creep damage in mullite tested in flexure

C. Baudín[a,*], M.P. Villar[b]

[a]*Instituto de Cerámica y Vidrio, 28 500, Arganda del Rey, Spain*
[b]*Departamento Ciencia de los Materiales, Ingeniería Metalúrgica y Química Inorgánica, Universidad de Cádiz, Cádiz, Spain*

Received 10 December 2001; received in revised form 20 March 2002; accepted 2 April 2002

Abstract

Creep damage of mullite, with nominal composition of $3Al_2O_32SiO_2$ and total impurity amount 0.63 wt.% including 0.11 wt.% Na_2O, was characterised in four point bending. Stresses from 40 to 130 MPa during 20 h were applied at 1200 °C. The samples tested at 130 MPa failed for shorter testing times (8–18 h). All samples experienced small strains (<0.14%) even before fracture. Microstructural characterisation of the post test samples was performed using SEM–EDX. Cracks that separated dense areas from the rest of the sample were observed close to the compression and tension surfaces. Quantitative evaluation of the size and distribution of these areas demonstrated that the observed damage increased systematically with the applied stress. Microchemical (EDX) analysis at the dense areas and cracks gave the phase compositions expected from the isothermal section at the testing temperature of the Al_2O_3–SiO_2–Na_2O ternary phase equilibrium diagram. In particular, high silica glasses with impurity accumulation and pure alumina were found. Microchemical analysis through the samples did not indicate that liquid migration occurred during testing. The reported data agree with enhanced dissolution of the mullite grains to take place at the stressed areas during creep tests.

Keywords: Creep; Damage; Failure analysis; Mullita; Microchemistry

1. Introduction

Mullite composition ranges from $3Al_2O_3{\cdot}2SiO_2$ to $2Al_2O_3SiO_2$ and is the only stable compound of the silica-alumina system under normal conditions of pressure and temperature.[1] Mullite has largely been known as one of the most common constituents of traditional ceramics. After the first data by Lessing et al.,[2] that reported a creep rate in compression of polycrystalline $3Al_2O_3.2SiO_2$ lower than that of alumina of the same grain size under the same experimental conditions, and Dokko et al.,[3] who found no plastic deformation of $2Al_2O_3{\cdot}SiO_2$ monocrystals under compression, much effort has been dedicated to the development of mullite materials for structural applications:[4–7] powder synthesis, processing, mechanical characterisation and toughening, and creep.

During the last 30 years, a wide range of creep activation energies (Q≈357–1051 kJ/mol), stress exponents (n≈0.2–2.7) and grain size exponents (P≈1–3.7) have been determined for mullite under stresses from 0.2 to 300 MPa and temperatures from 1100 to 1500 °C.[2–16] Mullite materials with different microstructures and compositions, from 67 to 82 wt.% of alumina, have been tested using different experimental conditions. In general, grain boundary sliding (GBS) is considered as the main deformation mechanism and that the strain rates are controlled by viscous flow of amorphous grain boundary phases, diffusion, solution-precipitation and/or cavitation. It is generally agreed that the broad range of reported creep parameters are due to differences in experimental conditions—loading arrangement, temperature and stress—as well as in microstructure and composition of the studied materials.

In a previous work,[16] the microstructural modifications of different nominally $3Al_2O_3{\cdot}2SiO_2$ polycrystalline mullites, during medium term (20 h) creep tests in 4-point bending at 1200 °C, were studied in order to understand why different stress exponents and

* Corresponding author. Tel.: +34-91-871-1800; fax: +34-91-870-0550.
E-mail address: cbaudin@icv.csic.es (C. Baudín).

0955-2219/02/$ - see front matter
PII: S0955-2219(02)00129-2

activation energies had been reported by different authors for the same mullites. All materials presented very little or no glassy phase at the grain boundaries. Special preparation of the samples for microstructural analysis by scanning electron microscopy was used in order to characterise the "as crept" parts of the samples located between the inner loading points and subjected to tension as well as compression during the creep experiments. In all materials highly dense zones with relatively large amounts of glass were observed close to the tension and compression surfaces. Viscous cavity growth was detected at depths (≈20–50 μm) from the tension and compression surfaces that varied from one material to the other. Strain values for all materials were very low and did not reflect the extreme microstructural modifications observed in the samples, and no significant cavitation was observed on polished and etched tensile surfaces of the samples.

In this work, the creep behaviour of the previously studied mullite with the lowest alkali content is further characterised. The aim was to analyse the distribution and characteristics of the observed microstructural modifications and whether a systematic relationship between the size of these modified areas and the applied stress could be found.

2. Experimental

The material MS,[16] made from commercial mullite powders (Chichibu Cement Co., Japan) was studied. Wet chemical analysis of the powder revealed that the alumina/silica molar ratio for this material is 1.57, and the following impurities were found: $ZrO_2 = 0.33$ wt.%, $TiO_2 = 0.13$ wt.%, $Na_2O = 0.11$ wt.%, $Fe_2O_3 = 0.03$ wt.%, $K_2O = 0.01$ wt.%, $MgO = 0.01$ wt.%, $Y_2O_3 = 0.01$ wt.%, $CaO = 0.002$ wt.%. The powders were isostatically pressed at 200 MPa into blocks and sintered (1650 °C–2 h). The lattice parameters of mullite in this sintered material correspond to a stoichiometric $3Al_2O_3{\cdot}2SiO_2$ mullite.

Polished and thermally etched surfaces of the as fabricated material were observed by analysed Scanning electron microscopy (SEM, Carl Zeiss DSM-950, Germany and 820 Jsm, Jeol, Japan), and the average grain size was determined by the linear intercept method assuming spherical particles on three areas of 100 μm^2.

Transmission electron microscopy (TEM) (Model 1200 EX TEM/STEM, Jeol, Japan) was performed on specimens prepared by wafering, mechanical thinning and dimpling, argon-ion milling and carbon coating.

For creep tests, bars ($3\times4\times50$ mm^3) were diamond machined from the sintered blocks using a standard water-oil emulsion as lubricant. Subsequently, samples were cleaned in deionised water in an ultrasonic bath. The surface to be in tension during the bending experiments was polished with diamond down to 6μm and chamfered using ethanol. Subsequently, samples were cleaned with ethanol in an ultrasonic bath.

Creep tests were performed at 1200 °C, in an universal load testing machine with an electrically heated furnace (INSTRON 6000, Great Britain) using 4-point bending fixtures made of alumina with inner and outer spans of 18 and 32 mm. Three levels of static stress (40, 100 and 130 MPa) were applied. At stress level 40 and 100 MPa tests duration of 20 h were used. Samples tested at 130 MPa failed at testing durations of 8–18 h. The central point deflection of the bars was measured using a SiC probe attached to a Linear Voltage Displacement Transducer through an alumina tube. Stress and strain were calculated by the procedure given by Hollenberg et al.[17] assuming a stress exponent of unity. No further corrections to the estimated stresses and strains were done. Therefore, the term apparent strain will be used in which follows.

For microstructural observations after testing, lateral surfaces perpendicular to the tension and compression surfaces, across the length of the samples, were embedded in resin and diamond polished down to 1 μm. The central parts, located between the outer loading points, of the samples tested under 40 and 100 MPa and the end parts of fractured samples tested at 130 MPa were observed. These cross section samples allowed to characterise the tension as well as the compression areas of the bars from the outer surfaces to the centre of the samples. Additional observations were performed on the fracture surfaces of samples tested under 130 MPa. As polished cross sections and fractured surfaces were gold sputtered and observed by scanning electron microscopy.

Microchemical analysis was done on polished and gold sputtered samples of the as fabricated material and the cross sections of the tested samples by energy dispersive X-ray analysis in the SEM (EDX, AN/10000, LINK, Great Britain). EDX analysis was carried on through the as fabricated material and cross section tested samples over equidistant areas of 5×5 μm^2 using 20 kV and 100 s as recording time. Semiquantitative calculations were done using the virtual standards of the equipment to compare the alumina/silica ratio in the as fabricated material with those through the cross sections of tested samples.

3. Results and discussion

Representative SEM and TEM micrographs and EDX analysis of the as fabricated mullite are shown in Fig. 1. The microstructure is bimodal with an average grain size of 1.2 μm (Fig. 1a). At the level of resolution employed most grain boundaries are clean (Fig. 1b) but some residual glass is observed located at triple points

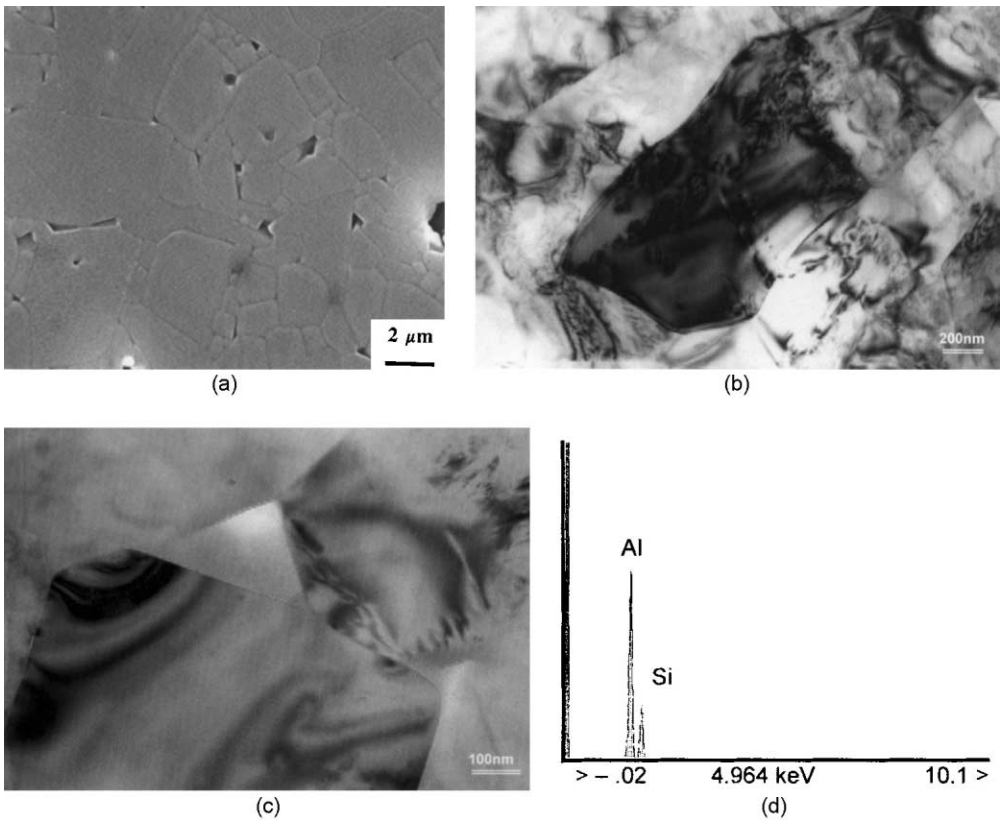

Fig. 1. Microstructural characteristics of the as fabricated mullite. (a) SEM micrograph of a polished and thermally etched (1500 °C–30 min) surface. (b) TEM. Aspect of the grains and clean grain boundaries. (c) TEM. Aspect of the grains and residual glass at triple points. (d) EDX analysis of 5×5 μm^2 areas across the sample.

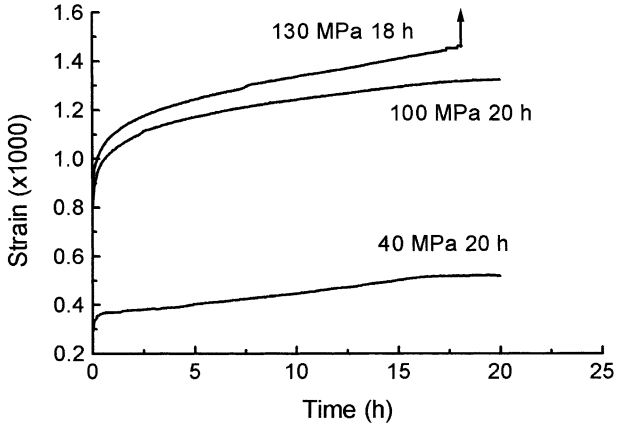

Fig. 2. Representative strain-time plots of samples tested at the indicated stresses.

(Fig. 1c). Only aluminium and silicon are detected in the analysis of 5×5 μm^2 areas across the bars before testing (Fig. 1d). This kind of microstructural development is characteristic of a structural mullite material with low impurity content.

In Fig. 2 representative strain-time plots are depicted. All samples experienced small apparent strains (<0.14%) even before fracture, as those determined by different authors for this mullite tested in bending under different experimental conditions.[8,16] The large range of apparent strain rates (10^{-12}–10^{-8} s^{-1}) observed for the stress interval of testing (40–140 MPa) indicates that a stress exponent higher than one describes the creep mechanism for this mullite, as determined previously using the stress jump technique.[13]

Microstructural analysis of the tested samples revealed the same kind of damage as previously reported[16] for several different mullites, constituted of dense areas with high glass content close to the tension and compression surfaces and separated from the rest of the sample by large cracks. Apparently, the extension of the damage was equal in the compression and tension areas and it was larger for larger stresses, but no quantitative analysis of the damage was done. In the previous work, it was proposed that viscous flow shrinkage at the highly stressed areas of the samples was responsible for densification.

The cracks observed in the cross sections are probably not formed during testing but during cooling of the samples from the testing temperature, due to differential thermal expansion behaviour. The location and size of these cracks is a result of the densification process which presumably occurred during testing. Therefore, low magnification observations were performed in order to analyse the distribution of the cracks.

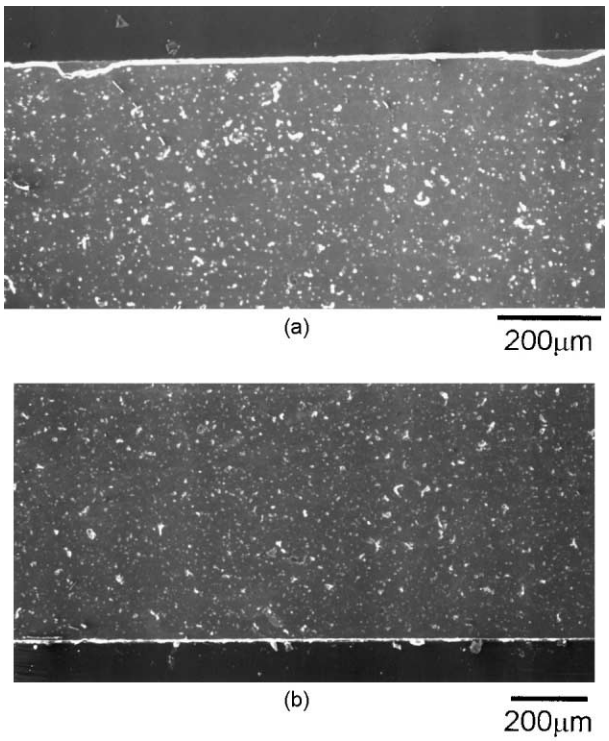

Fig. 3. Representative low magnification micrographs of cross sections of a sample tested at 40 MPa during 20 h. Both micrographs correspond to portions of the sample located at the same longitudinal position. (a) Portion close to the compression surface (upper part of the micrograph), showing damage. (b) Portion close to the tension surface (lower part of the micrograph), showing no damage.

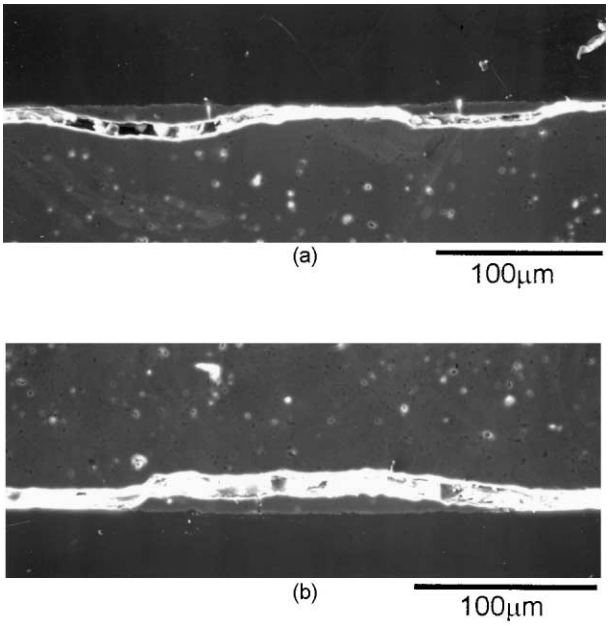

Fig. 4. Representative low magnification micrographs of cross sections of a sample tested at 100 MPa during 20 h. Both micrographs correspond to portions of the sample located at the same longitudinal position. (a) Portion close to the compression surface (upper part of the micrograph), showing damage. (b) Portion close to the tension surface (lower part of the micrograph), showing more severe damage than in compression.

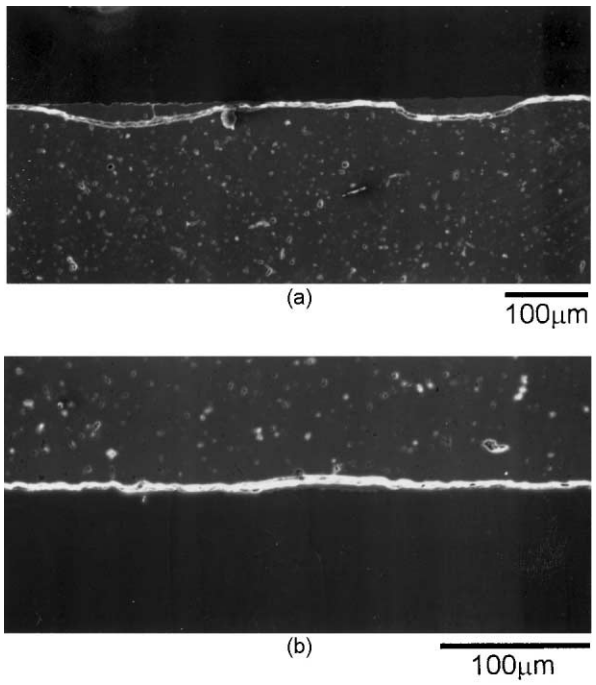

Fig. 5. Representative low magnification micrographs of cross sections of a sample tested at 130 MPa during 17 h. Both micrographs correspond to portions of the sample located at the same longitudinal position. (a) Portion close to the compression surface (upper part of the micrograph), showing damage. (b) Portion close to the tension surface (lower part of the micrograph), showing less severe damage than in compression.

Representative low magnification micrographs of the cross sections of tested samples are shown in Figs. 3–5. In all cases, cracks were found through the whole portions of the samples between the outer loading points and located in the areas close to the compression surfaces (Figs. 3–5a) as well as close to the tension surfaces (Figs. 3–5b). There was not a systematic spatial correlation between the tension and compression cracks. In some cases, damaged areas close to the tension/compression surfaces were located at the same longitudinal position of the sample as undamaged areas close to the compression/tension surface (Fig. 3). In other cases, the severity of the damage was very different at corresponding tension/compression areas (Figs. 4 and 5), as will be discussed further.

Accumulation of cracks occurred in the areas close to the fracture lines of the samples tested at 130 MPa (Fig. 6a). In the fracture surfaces of these samples no differentiated fracture origins but large process areas were observed (Fig. 6b and c). Highly dense zones were found close to the tension surface followed by partially dense zones at larger distances from the tension surfaces.

Apparently, crack density was also larger in the central parts of the samples tested at lower stresses (40 and 100 MPa). In order to quantify this qualitative observation, cracks were characterised by two parameters: length and depth were defined as the maximum dimensions of

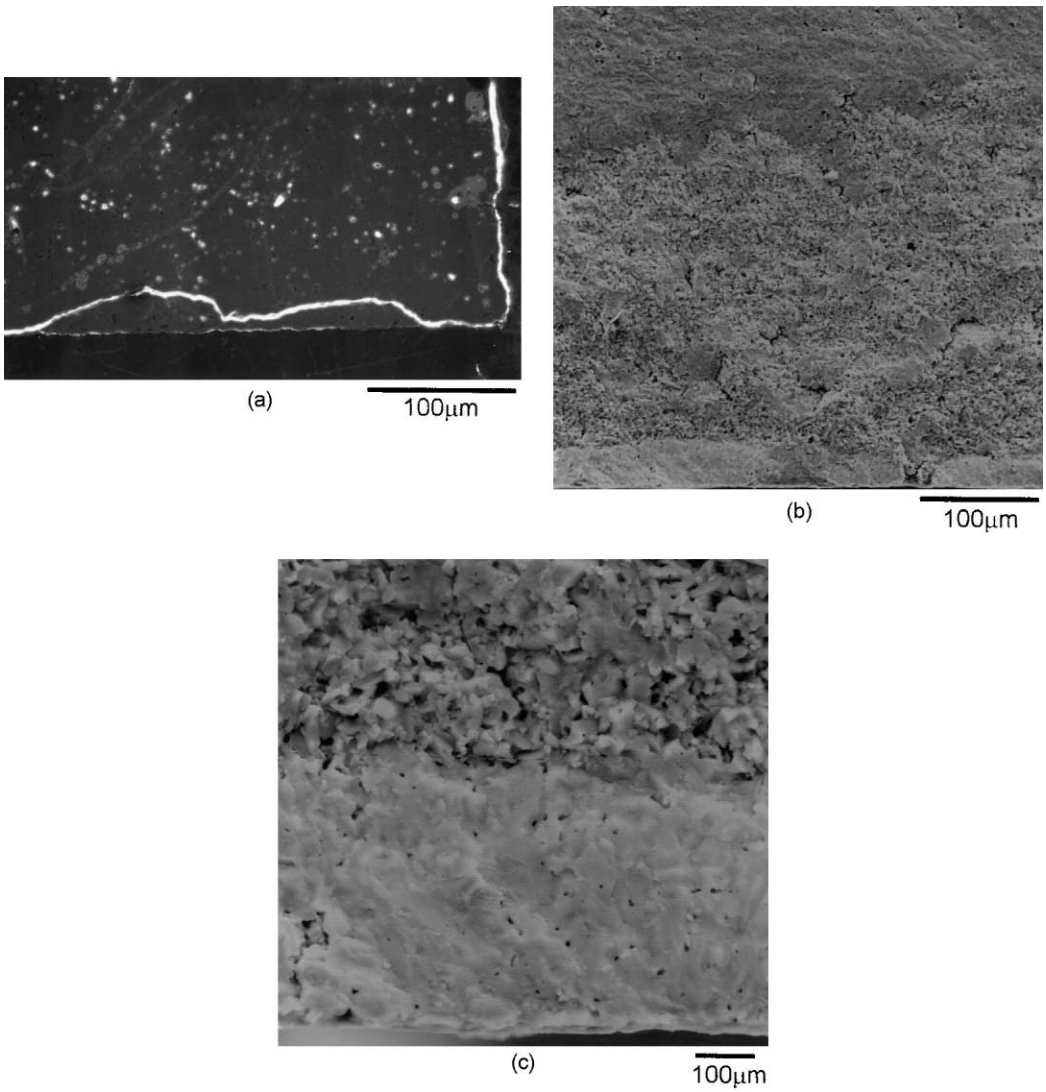

Fig. 6. SEM micrographs of samples failed during testing. (a) Cross section of a sample tested at 130 MPa during 17 h. Accumulation of damage close to the fracture line (right end) is observed. (b) Low magnification of the fracture surface of a sample tested at 130 MPa during 8 h. The process zone close to the tension surface (lower part of the micrograph) is observed. (c) Higher magnification of the fracture surface of Fig. 6b. The high density zone close to the tension surface and the partially dense zone close located at larger distances from the tension surface are observed.

the crack parallel and perpendicular to the sample tension and compression surfaces, respectively.

Fig. 7 shows creep damage diagrams as a function of sample length for two samples tested at 40 and 100 MPa during 20 h and one sample tested at 130 MPa during 17 h. Even though a larger amount of deeper cracks is found towards the central portions of the samples, local damage occurs in the portions between the outer and inner loading points, specially in the samples tested at 100 and 130 MPa.

Table 1 summarises the data from Fig. 7. Crack density has been defined as total crack length/sample length

Table 1
Quantiative evaluation of the creep damage diagrams (Fig. 7)

Sample	Crack density (%)		Crack length [standard deviation] (μm)		Crack depth [standard deviation] (μm)	
	Compression	Tension	Compression	Tension	Compression	Tension
40 MPa—20 h	8	9	168 [103]	158 [131]	16 [8]	18 [10]
100 MPa—20 h	11	12	184 [107]	172 [108]	24 [10]	24 [5]
130 MPa—17 h	18	↑	235 [280]	265 [300]	23 [14]	↑

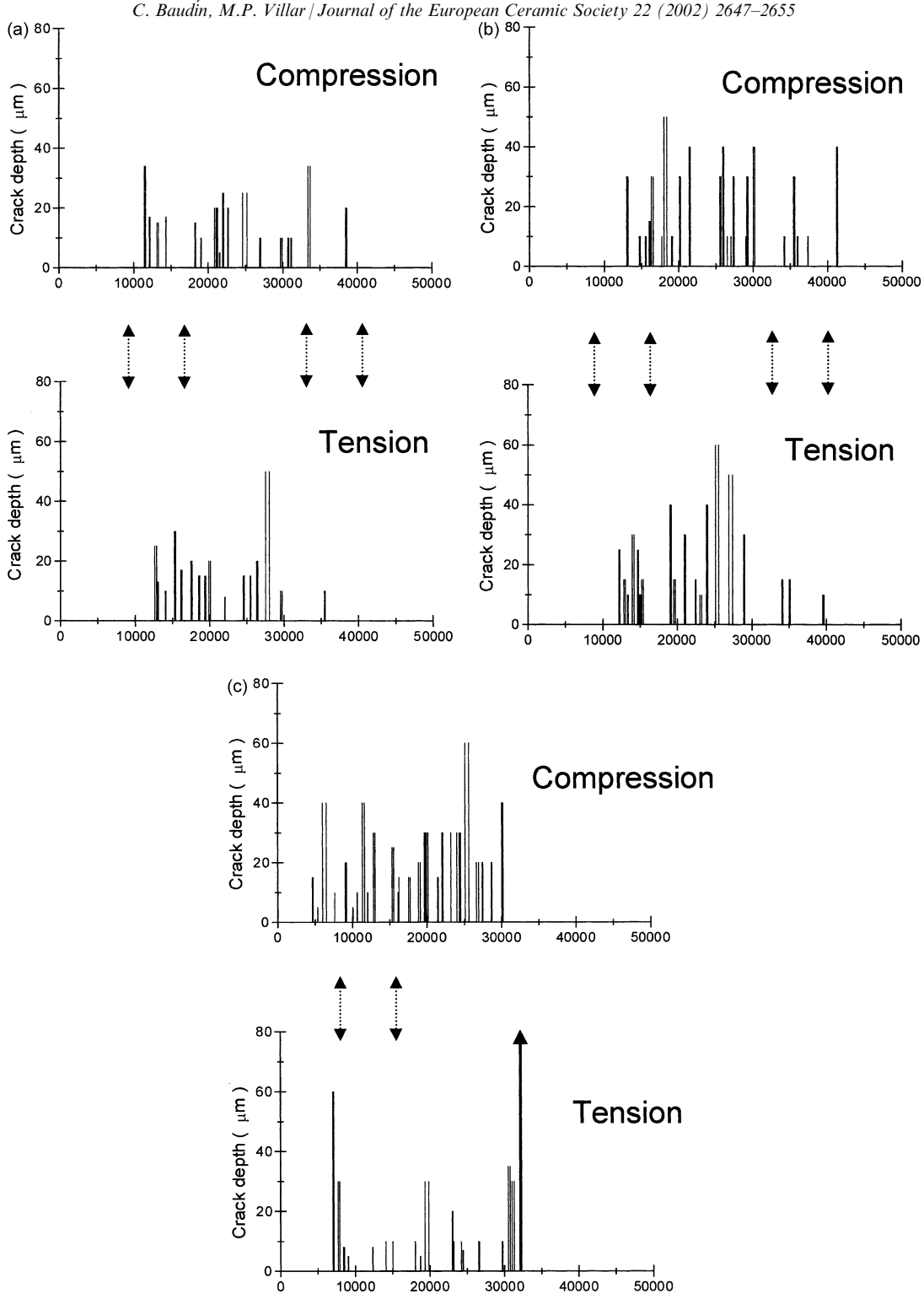

Fig. 7. Creep damage diagrams as a function of sample length. The thick lines indicate the observed length of the sample and the arrows indicate the loading points. (a) Sample tested at 40 during 20 h. (b) Sample tested at 100 MPa during 20 h. (c) Sample tested at 130 MPa during 17 h.

between the outer loading points. Average crack length and depth have been calculated taking into account all cracks. No significant differences exist between data for tension and compression areas, but for the sample tested at 130 MPa which failed. Crack length and density increase with testing stress. Crack depth experiences a significant increase when stress increases from 40 to 100 MPa. The samples tested at 100 and 130 MPa present similar values of crack depth, except for the fracture zone in the sample tested at 130 MPa.

All these observations indicate that this mullite experiences creep damage due to the combined compression/

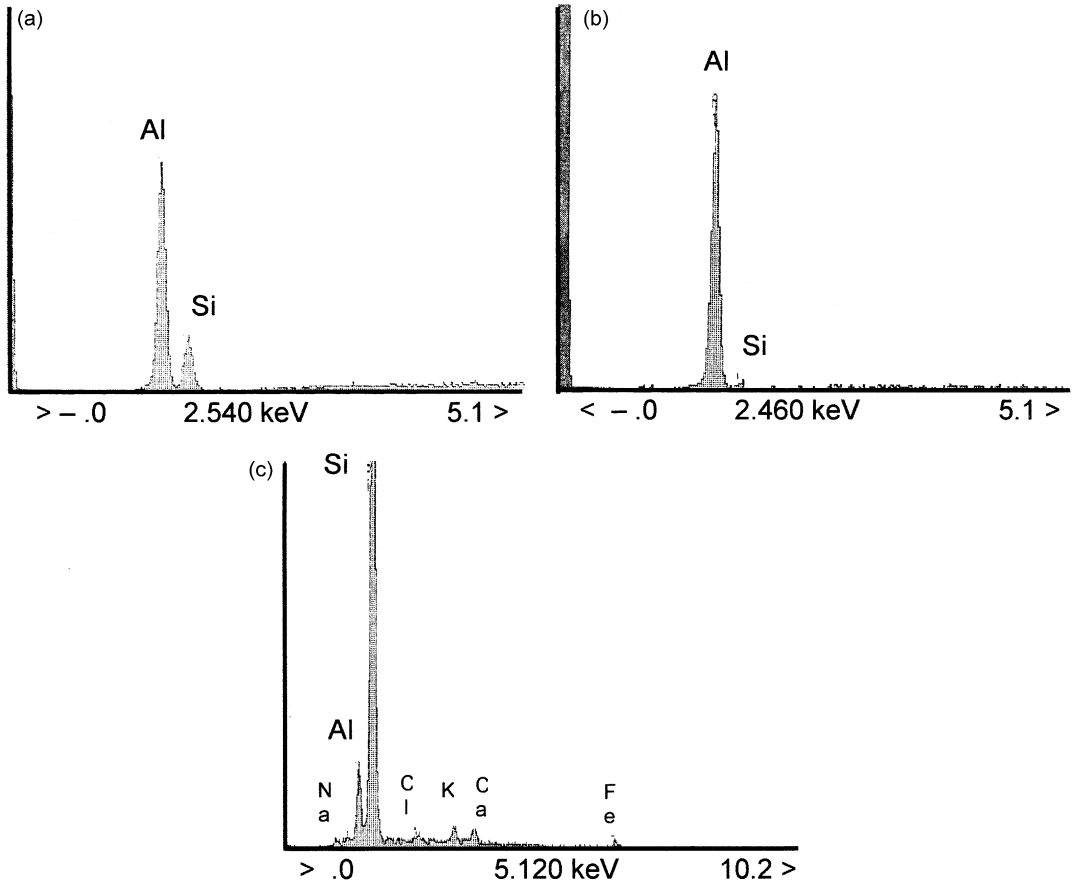

Fig. 8. Representative EDX analysis of tested samples. (a) 5×5 μm^2 areas across the samples and point analysis around the cracked areas. Only aluminium and silicon are present. Original mullite. (b) Point analysis of the cracked areas. Alumina local composition. (c) Point analysis of the cracked areas. High silica regions in which impurities—Na, K, Ca, Fe—are detected.

tension stress state developed in bending tests as well as due to the singularity of the stress state developed at the loading points. The increase of the size and density damage parameters with stress demonstrate that the damage observed in the samples is directly related to creep testing.

In Fig. 8, characteristics EDX analysis of cross sections of tested samples are shown. No significant differences (<1%) were found between compositions of 5×5 μm^2 areas across the samples, only aluminium and silicon were detected, and the analyses (Fig. 8a) were coincident with those of the as fabricated samples (Fig. 2d). The same composition was also found locally around the cracked areas by point analysis. Point analysis inside the cracks (Fig. 8b and c) gave variable compositions, from that of the original mullite to nearly that of alumina (Fig. 8b) without impurities. Impurity—Na, K, Ca, Fe—accumulations were detected locally in high silica regions (Fig. 8c), such as those vitrified regions observed in different mullites.[16]

Even though pure mullite is a highly refractory oxide, in which no liquid formation is expected up to 1595 °C,[1] most of the impurities detected in the mullite studied here (CaO, K_2O, Na_2O, Fig. 8c) lead to a decrease in the temperatures for liquid formation, when the ternary equilibrium is considered.[18–21] These temperatures are further decreased by the combined action of several impurities. Moreover, as impurities are mostly located at grain boundaries it is not the average composition of the powder (total content of liquid forming impurities ≈0.12 wt.%) which is playing a role but the local compositions at the grain boundaries.

In the material studied here, the impurity that is present in a major amount is Na_2O, therefore, the Al_2O_3–SiO_2–Na_2O system[20] may be used as first approximation for discussion. Similar predictions arise from the Al_2O_3–SiO_2–K_2O[19] diagram. Phase relationships are more complicated when the Al_2O_3–SiO_2–CaO[18] system is taken into account, but the invariant points in this system are higher than the testing temperature. Fig. 9 shows a schema of the isothermal section of the Al_2O_3–SiO_2–Na_2O at the testing temperature (1200 °C). Grain boundary compositions in the studied material may be located at three different tie triangles. For high silica-low impurity grain boundaries the equilibrium phase composition is mullite + cristobalite + a liquid, L1, with

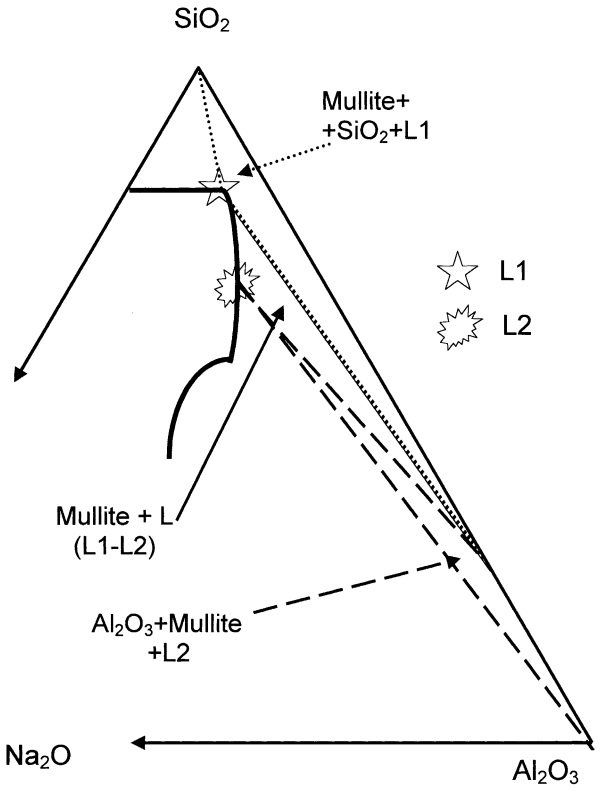

Fig. 9. Schema of the isothermal section of the Al_2O_3–SiO_2–Na_2O phase equilibrium diagram at the testing temperature (1200 °C). The phase compositions corresponding to each tie triangle are indicated. L1 and L2 are liquid compositions discussed in the text.

about 82, 12 and 6 wt.% of SiO_2, Al_2O_3 and Na_2O, respectively. For high alumina or higher impurity content, the corresponding one is α-alumina + mullite + a liquid, L2, with lower silica content (≈72 wt.%) and larger amounts of alumina (≈18 wt.%) and Na_2O (≈10 wt.%). For the compositions located between these two tie triangles, mullite + a liquid which composition may change between L1 and L2, depending on the particular grain boundary composition, will be formed.

At temperatures higher than 1200 °C, such as the sintering temperature (1650 °C), high silica compositions will lead to liquids with higher silica contents whereas for the high alumina compositions the alumina content in the liquids will increase. The former ones are high viscosity liquids that, in principle, will not migrate at the testing temperature. The viscosity of the later decrease for decreasing silica contents and, therefore, these liquids might migrate towards the sample surfaces during testing. This migration would imply a compositional variation across the sample, leading to higher alumina contents in the areas close to the surfaces which, at least at the experimental conditions used (EDX) have not been found (Figs. 1d and 8a). From the above phase equilibrium relations, local compositions such as those plotted in Fig. 8 will be expected for this mullite annealed at 1200 °C. Therefore, liquid formation is expected during testing. Also part of these liquids, formed through the whole sample, could migrate towards the surfaces. But this will also produce a change in composition across the sample which, as discussed above, has not been found.

In summary, data suggest that preferential mullite decomposition into the equilibrium phases occurs in the highly stressed areas of the samples. A similar effect has been described for creep testing of a mullite-alumina fibre with Na_2O at temperatures from 1200 to 1500 °C.[22,23] In this fibre, decomposition of mullite into alumina and a silica rich liquid during testing was observed. The reported observations are in good agreement with predictions from Fig. 9, as the fibre composition would be located in the alumina rich tie triangle. In the material studied here, alumina was formed only locally (Fig. 8b), depending on the particular grain boundary composition.

Differential densification of the areas of the samples with larger amounts of liquid, can be explained in terms of the viscous cavity growth model, as proposed in the previous work.[16] Considering the viscosity and the surface energy of the liquid constant for the same material, shrinkage of the cavities will be enhanced for larger stresses. Therefore, larger dense areas are expected in the samples subjected to increasing stresses. Quantitative data from Fig. 7 and Table 1 demonstrate this fact.

Many creep data of ceramics have been obtained in flexure tests. It is generally assumed that creep behaviour can be completely characterised from the strain-time plots and microstructural analysis of the tension surface of the samples, considering only the portion located under the central loading point in three point bending tests or between the inner loading points in four point bending tests. Data from this study indicate that damage extension occurs across the whole portions of the samples subjected to the complicate stress state developed in bending.

4. Conclusions

Creep damage in bending of a high purity and dense mullite with nominal composition $3Al_2O_32SiO_2$ was characterised. Dense areas differed from the rest of the sample by cracks that were close to the compression and tension surfaces. Quantitative evaluation of the size and spatial distribution of these areas has demonstrate that the observed damage increases systematically with testing stress and that damage occurs in the whole portions of the samples located between the outer and inner loading points. This was more pronounced in the samples tested at the higher stresses (100–130 MPa).

EDX analysis at the dense areas and regions with cracks gave the phase compositions expected from the ternary phase equilibrium diagrams when impurities are

taken into account. In particular, high silica glasses with impurity accumulation and pure alumina were found. The analysis through the samples did not indicate that liquid migration occurred during testing. The reported data agree with stress enhanced dissolution of the mullite grains to take place at the stressed areas during creep tests. Exhaustive microstructural analysis of samples tested under a homogeneous stress state—pure compression or tension—would be needed to clarify the creep damage mechanisms in stoichiometric $3Al_2O_32$-SiO_2 mullites.

Acknowledgements

This work was supported by CICYT (Spain), Contract MAT00–0949. The authors wish to thank Professor S. de Aza, Dr. P. Pena and Dr. M.J. Kramer for helpful discussions.

References

1. Klug, F. J., Prochatzka, S. and Doremus, R. H., Alumina-silica phase diagram in the mullite region. *J. Am. Ceram. Soc.*, 1987, **70**(10), 750–759.
2. Lessing, P. A., Gordon, R. S. and Mazdiyasni, K. S., Creep of polycrystalline mullite. *J. Am. Ceram. Soc.*, 1975, **58**(3–4), 149.
3. Dokko, P. C., Pask, J. A. and Mazdiyasni, K. S., High-temperature mechanical properties of mullite under compression. *J. Am. Ceram. Soc.*, 1977, **60**(3–4), 150–155.
4. Somiya, S., Davies, R. F. and Pask, J. A., *Ceram. Trans., vol. 6, Mullite and Mullite Matrix Composites*. The Am. Ceram. Soc.Inc, Westerville OHIO, 1990.
5. Schneider, K., Okada, J. A. and Pask, J. A., *Mullite and Mullite Ceramics*. John Wiley & Sons Ltd, West Sussex, Great Britain, 1994.
6. Mullite 94, Special issue *J. Eur. Ceram. Soc.*, 1996, **16** (2).
7. Mullite 2000, Refereed reports, *J. Eur. Ceram. Soc.*, 2001, **21** (14).
8. Penty, R. A. and Hasselman, D. P. H., Creep kinethics of high purity, ultra-fine grain polycrystalline mullite. *Mater. Res. Bull.*, 1972, **7**(10), 1117–1124.
9. Okamoto, Y., Fukudome, H., Hayashi, K. and Nishikawa, T., Creep deformation of polycrystalline mullite. *J. Eur. Ceram. Soc.*, 1990, **6**(1), 161–168.
10. Torrecillas, R., *Comportamiento Mecánico de Mullita Y Mullita-Circona Obtenida por Sinterización Reactiva*. PhD thesis, Universidad Nacional de Educación a Distancia, Madrid, Spain, 1990.
11. Jakus, K. and Wiedehorn, S. M., Creep deformation of ceramics in four-point bending. *J. Am. Ceram. Soc.*, 1988, **71**(10), 832–836.
12. Ashizuka, M., Honda, T. and Kubota, Y., Effects of grain size on creep of mullite ceramics. *J. Ceram. Soc. Jpn. Int. Ed.*, 1991, **99**(4), 282–285.
13. Baudín, C., Osendi, M. I., Descamps, P. and Cambier, F., High temperature mechanical properties and creep behaviour of different mullites. In *Key Engineering Materials, vol. 132, Euro Ceramics V*, ed. P. Abelard, M. Boussuge, Th. Chartier, G. Fantozzi, G. Lozes and A. Rousset. Trans Tech. Publications, Switzerland, 1997, pp. 591–594.
14. Torrecillas, R., Calderón, J. M., Moya, J. S., Reece, M. J., Davies, C. K. L., Olagnon, C. and Fantozzi, G., Suitability of mullite for high temperature applications. *J. Eur. Ceram. Soc.*, 1999, **19**(11), 2519–2527.
15. Hynes, A. P. and Doremus, R. H., High-temperature compresive creep of polycrystalline mullite. *J. Am. Ceram. Soc.*, 1991, **74**(10), 2469–2475.
16. Fernandez, E. and Baudín, C., Creep damage in different $3Al_2O_3{\cdot}2SiO_2$ mullites tested in 4-point bending. *J. Eur. Ceram. Soc.*, 2001, **21**(12), 2243–2251.
17. Holleberg, G. W., Terwillinger, G. R. and Gordon, R. S., Calculation of stresses and strains in four-point bending creep tests. *J. Am. Ceram. Soc.*, 1971, **54**(4), 196–199.
18. Osborn, E. F. and Muan, A., Fig. 631. In *Phase Diagrams for Ceramists*, ed. E. M. Levin, C. R. Robbins and H. F. McMurde. American Ceramic Society, Columbus, OH, 1964.
19. In Ref 18, Fig. 401.
20. In Ref 18, Fig. 501.
21. Baudín, C. and Villar, M. P., Influence of thermal aging on microstructural development of mullite containing alkalis. *J. Am. Ceram. Soc.*, 1998, **81**(10), 2741–2745.
22. Deléglise, F., Berger, M. H., Jeulin, D. and Bunsell, A. R., Microstructural stability and room temperature mechanical properties of the Nextel 720 fibre. *J. Eur. Ceram. Soc.*, 2001, **21**(5), 569–580.
23. Deléglise, F., Berger, M. H. and Bunsell, A. R., Microstructural evolution under load and high temperature deformation mechanisms of a mullite/alumina fibre. *J. Eur. Ceram. Soc.*, 2002, **22**, 1501–1512.